Progress In Electromagnetics Research, PIER 38, 1–27, 2002

A HYBRID FDFD-BIE APPROACH TO TWO-DIMENSIONAL SCATTERING FROM AN INHOMOGENEOUS BIISOTROPIC CYLINDER

M. Norgren

Division of Electromagnetic Theory
Alfvén Laboratory
Kungliga Tekniska Högskolan, SE-100 44 Stockholm, Sweden

Abstract—The scattering problem for an inhomogeneous two-dimensional biisotropic cylinder is solved in the frequency-domain by means of a hybrid method, in which finite difference equations in the interior region are combined with a mesh truncation in terms of a boundary integral equation that realizes a global absorbing boundary condition. The influences of the chirality and non-reciprocity parameters on the scattering properties are investigated. Numerical results for the bistatic echo widths are presented and compared with a reference solutions in the circular cases and it is found that the method yields more accurate results than what can be achieved with a local absorbing boundary condition. It is realized that, for a given mesh, the method presented is computationally slower than a method based on a local absorbing boundary condition but in on the other hand the method is much faster than the readily used method of moments. The present method is thus suitable for solving scattering problems involving scatterers of intermediate sizes.

1. INTRODUCTION

1 Introduction

An electromagnetic scattering problem involving scatterers consisting of penetrable inhomogeneous linear media can be formulated as a volume integral equation (VIE). For the numerical implementation, the VIE is discretized into a linear matrix equation by using the method of moments (MoM) [1], where for isotropic media the derivation of the VIE and the numerical implementation using MoM are described in e.g., [2]. Extensions of the VIE formulation to chiral and bianisotropic media can be found in [3] and [4], respectively. The advantage of the VIE approach is that it provides a general framework applicable to all kinds of linear media, and that the radiation condition for the scattered fields is inherent in the dyadic Green's function. The drawback of VIE is that the global integral operator discretizes into an entirely filled matrix. Thus, for a problem with a geometry several wavelengths in size the matrix will require a large amount of storage and it becomes exceedingly time consuming to invert it.

An alternative to the VIE approach is to use a partial differential equation (PDE) method, in which the differential operator is discretized by using finite differences (FD) or by using the finite element method (FEM). The local differential operator discretizes into a sparsely filled matrix that can be inverted fast and requires a small amount of storage. However, when using FD or FEM in an open region a radiation condition must be supplemented separately by truncating the computational domain with an absorbing boundary condition (ABC), which can be either an approximate (local) ABC or an exact (global) ABC. An example of a local ABC is the perfectly matched layer (PML), which has been used for the finite difference time domain (FDTD) method [5], the finite element frequency domain (FEFD)

method [6] and the finite difference frequency domain (FDFD) method [7]. PML has been extended to include biisotropic and bianisotropic media also [8, 9]. Another approach to a local ABC is the measured equation of invariance (MEI), in which a local operator at the boundary is determined by adaption, in an overdetermined sense, to the fields generated by a number of possible sources located inside the domain of the scatterer. MEI has been used in conjunction with FDFD in [10–12]. A global ABC is usually formulated in terms of an integral operator on the boundary of the domain enclosing the scatterer, which yields that the FD or FEM equations then must be solved in conjunction with a boundary integral equation (BIE) that has been discretized using MoM; see e.g., the method described in [13] in which the Laplace equation is solved by combining FD with a BIE. Other examples of such combined methods, referred to as hybrid methods, are e.g., FEM-BIE [14–16] and FDTD-BIE [17].

The main advantage using a local ABC in a numerical PDE method based on matrix inversion is that the sparsity in the matrix will be preserved, which results in a fast inversion, whilst a global ABC yields a filled submatrix that slows down the matrix inversion considerably unless the inversion can be accelerated by means of e.g., a transform method [15, 16, 18]. On the other hand, a local ABC is usually adapted to the shape of the scatterer [10] and is therefore unreliable if one has no prior information about the shape, which might be the case if one uses the solver iteratively in an optimization procedure in order to solve e.g., an inverse problem. Since an inverse problem usually is illposed, it is also very important that one uses a very accurate ABC since artifacts from the boundary of the computational domain, due to a poor ABC, will literally hinder the sight between the scatterer and the measurement point, which then easily leads to a corrupted solution.

In this paper, we consider a hybrid FDFD-BIE approach to the two-dimensional scattering problem for an inhomogeneous cylinder of a biisotropic material. A biisotropic material is in general both chiral and non-reciprocal, thus requiring two additional constitutive parameters besides the usual permittivity and permeability. For a comprehensive description of biisotropic media and its applications, we refer to the text book [19]. Interior to the region containing the biisotropic cylinder, we use a FDFD scheme similar to the ones presented in [11, 12] and on the boundary of the region we use a BIE which, in the two-dimensional case, reduces to a contour integral equation. It should be noted that the BIE method has been exploited earlier for scattering from homogeneous biisotropic objects, in both the two-dimensional [20] and the three-dimensional case [21].

The paper is organized as follows. In Section 2, the scattering problem is formulated and the basic equations are derived. In Section 3, we extend the finite difference equations for isotropic media [11] to include biisotropic media as well. In Section 4, we describe the integral equation for the global ABC and how it is connected to the FD equations. Numerical results for the bistatic echo widths are presented in Section 5 and in Section 6 we present some conclusions.

2. THE SCATTERING PROBLEM

Consider a bounded, inhomogeneous and biisotropic object, henceforth the scatterer, located in free space; see Figure 1. The scatterer is described by the following biisotropic constitutive relations in the frequency-domain [19]:

$$\boldsymbol{D}(\boldsymbol{r}) = \varepsilon_0 \varepsilon(\boldsymbol{r}) \boldsymbol{E}(\boldsymbol{r}) + \sqrt{\varepsilon_0 \mu_0}\, \xi(\boldsymbol{r}) \boldsymbol{H}(\boldsymbol{r}), \tag{1}$$

$$\boldsymbol{B}(\boldsymbol{r}) = \mu_0 \mu(\boldsymbol{r}) \boldsymbol{H}(\boldsymbol{r}) + \sqrt{\varepsilon_0 \mu_0}\, \zeta(\boldsymbol{r}) \boldsymbol{E}(\boldsymbol{r}), \tag{2}$$

where ε is the relative permittivity, μ is the relative permittivity, and where ξ and ζ are the magnetoelectric cross-coupling parameters; ε_0 and μ_0 are the permittivity and permeability of vacuum, respectively. As the scatterer is inhomogeneous, ε, μ, ξ and ζ are arbitrary functions of the position variable $\boldsymbol{r}$.

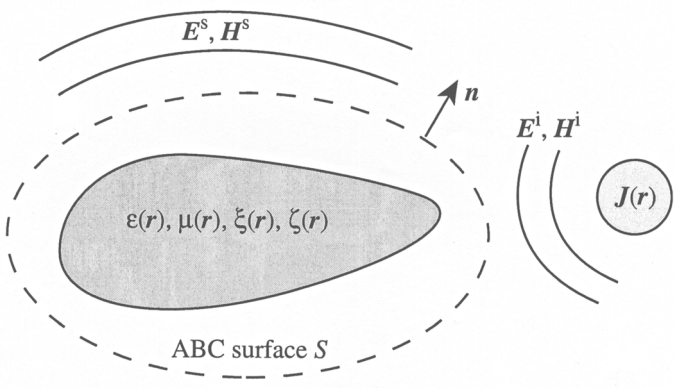

Figure 1. The scattering configuration.

The scattering problem is to determine the scattered fields, $\{\boldsymbol{E}^{\mathrm{s}}, \boldsymbol{H}^{\mathrm{s}}\}$, when the scatterer is excited by known incident fields, $\{\boldsymbol{E}^{\mathrm{i}}, \boldsymbol{H}^{\mathrm{i}}\}$, created by a time-harmonic (exp $(j\omega t)$) current density $\boldsymbol{J}$

located exterior to the scatterer; see Figure 1. Substituting the constitutive relations (1) and (2) into the Maxwell's equations

$$\nabla \times \boldsymbol{E} = -\mathrm{j}\omega \boldsymbol{B}, \qquad \nabla \times \boldsymbol{H} = \mathrm{j}\omega \boldsymbol{D} + \boldsymbol{J}, \tag{3}$$

we obtain

$$\nabla \times \boldsymbol{E} = -\mathrm{j}k_0(\eta_0 \mu \boldsymbol{H} + \zeta \boldsymbol{E}), \quad \nabla \times \boldsymbol{H} = \mathrm{j}k_0 \left(\eta_0^{-1} \varepsilon \boldsymbol{E} + \xi \boldsymbol{H}\right) + \boldsymbol{J}, \tag{4}$$

where $k_0 = \omega\sqrt{\varepsilon_0 \mu_0}$ and $\eta_0 = \sqrt{\mu_0/\varepsilon_0}$ are the wave number and intrinsic wave impedance in vacuum, respectively. To o tain numerical balance betwee the fields $\boldsymbol{E}$ and $\boldsymbol{H}$, we henceforth rescale the $\boldsymbol{H}$-field as $\eta_0 \boldsymbol{H} \to \boldsymbol{H}$. Thus, sequel (4) becomes

$$\nabla \times \boldsymbol{E} = -\mathrm{j}k_0(\mu \boldsymbol{H} + \zeta \boldsymbol{E}), \tag{5}$$

$$\nabla \times \boldsymbol{H} = \mathrm{j}k_0(\varepsilon \boldsymbol{E} + \xi \boldsymbol{H}) + \eta_0 \boldsymbol{J}. \tag{6}$$

3. THE FDFD EQUATIONS

In this section, we derive the FDFD equations in the two-dimensional case. The FDFD scheme is of the same type as the ones presented in [11, 12]. With no dependence on the z-coordinate, we have

$$\boldsymbol{r} = x\hat{\boldsymbol{x}} + y\hat{\boldsymbol{y}}, \qquad \nabla = \nabla_{\mathrm{T}} \equiv \hat{\boldsymbol{x}}\frac{\partial}{\partial x} + \hat{\boldsymbol{y}}\frac{\partial}{\partial y},$$

where $\hat{\boldsymbol{x}}$ and $\hat{\boldsymbol{y}}$ denote the transversal unit-vectors in the cartesian coordinate system.

The region containing the scatterer is divided into quadratic cells, where in each cell the constitutive parameters are approximated as homogeneous and equal to their true values at the center of the cell; see Figure 2. Taking the curls of Equations (5) and (6) in a homogeneous and source-free ($\boldsymbol{J} = \boldsymbol{0}$) region and using the same equations again to eliminate all single curl terms, we obtain in each cell the following second order equations for the fields:

$$\left[\nabla_{\mathrm{T}}^2 + k_0^2\left(\varepsilon\mu - \zeta^2\right)\right]\boldsymbol{E} + k_0^2\mu(\xi - \zeta)\boldsymbol{H} = \boldsymbol{0}, \tag{7}$$

$$\left[\nabla_{\mathrm{T}}^2 + k_0^2\left(\varepsilon\mu - \xi^2\right)\right]\boldsymbol{H} + k_0^2\varepsilon(\zeta - \xi)\boldsymbol{E} = \boldsymbol{0}. \tag{8}$$

Here we have also used that the divergences of (5) and (6), in a homogeneous and source- free region, imply $\nabla_{\mathrm{T}} \cdot \boldsymbol{E} = \nabla_{\mathrm{T}} \cdot \boldsymbol{H} = \boldsymbol{0}$, provided the condition

$$\varepsilon\mu - \xi\zeta \neq 0 \tag{9}$$

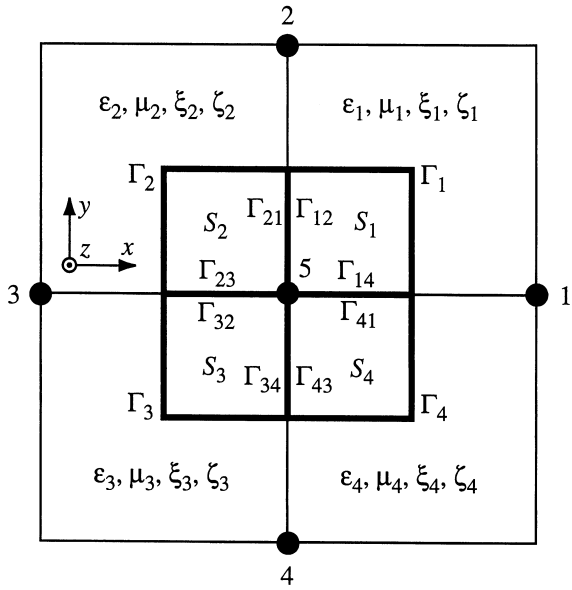

Figure 2. The locations of the FDFD nodes above the piecewise homogeneous approximation of the constitutive parameters.

holds. The condition (9) is very sound physically [22, 19] and will be assumed throughout. Obviously, (7) and (8) are satisfied individually by the cartesian field-components. However, since the field-components in the z-direction are tangential to all boundaries between the cells, and thereby continuous, it is advantageous to use the z-components of Equations (7) and (8) for the finite difference approximations.

Following [11], the fields are evaluated at the intersection points between the cell boundaries. The square region containing all points closest to a certain evaluation point is divided into four quadrants, for which $S_i, i = 1, 2, 3, 4$ denote the cross-sections and $\Gamma_i, i = 1, 2, 3, 4$ denote the corresponding boundaries; see Figure 2. Integrating the z-components of (7) and (8) over the cross-section of the i:th quadrant and employing the theorem of Gauss, we obtain

$$\oint_{\Gamma_i} \frac{\partial E_z}{\partial n_i} \mathrm{d}l + k_0^2 \int_{S_i} \left[\left(\varepsilon_i \mu_i - \zeta_i^2 \right) E_z + \mu_i (\xi_i - \zeta_i) H_z \right] \mathrm{d}S = 0, \qquad (10)$$

$$\oint_{\Gamma_i} \frac{\partial H_z}{\partial n_i} \mathrm{d}l + k_0^2 \int_{S_i} \left[\left(\varepsilon_i \mu_i - \xi_i^2 \right) H_z + \varepsilon_i (\zeta_i - \xi_i) E_z \right] \mathrm{d}S = 0. \qquad (11)$$

Approximating the normal derivatives on the parts of the boundaries that passes within the cell with central differences, the numerical approximation of equation (10) in the first quadrant becomes

$$\frac{E_{z1}-E_{z5}}{h}\cdot\frac{h}{2}+\frac{E_{z2}-E_{z5}}{h}\cdot\frac{h}{2}+\int_{\Gamma_{12}}\frac{\partial E_z}{\partial n_1}\mathrm{d}l+\int_{\Gamma_{14}}\frac{\partial E_z}{\partial n_1}\mathrm{d}l + \left(\frac{k_0 h}{2}\right)^2\left[\left(\varepsilon_1\mu_1-\zeta_1^2\right)E_{z5}+\mu_1(\xi_1-\zeta_1)H_{z5}\right]=0 \qquad (12)$$

where h is the side-length of the cells and where Γ_{12} and Γ_{14} denote the interfaces to the adjacent quadrants around the evaluation point; see Figure 2. The corresponding equations for the other quadrants, are obtained by cyclic permutation of the indices ($1234 \rightarrow 2341$ etc.). By introducing the following abbreviations:

$$q=\frac{k_0 h}{2},\qquad \Gamma_{ij}^{\mathrm{E}}=\int_{\Gamma_{ij}}\frac{\partial E_z}{\partial n_i}\mathrm{d}l,\qquad \Gamma_{ij}^{\mathrm{H}}=\int_{\Gamma_{ij}}\frac{\partial H_z}{\partial n_i}\mathrm{d}l, \qquad (13)$$

Equations (10) and (11) in the first quadrant are written as (cyclic permutation yields the equations for the other quadrants)

$$-\Gamma_{12}^{\mathrm{E}}-\Gamma_{14}^{\mathrm{E}}=\frac{1}{2}(E_{z1}+E_{z2})+\left[q^2\left(\varepsilon_1\mu_1-\zeta_1^2\right)-1\right]E_{z5}+q^2\mu_1(\xi_1-\zeta_1)H_{z5} \equiv A_1^{\mathrm{E}} \qquad (14)$$

$$-\Gamma_{12}^{\mathrm{H}}-\Gamma_{14}^{\mathrm{H}}=\frac{1}{2}(H_{z1}+H_{z2})+\left[q^2\left(\varepsilon_1\mu_1-\xi_1^2\right)-1\right]H_{z5}+q^2\varepsilon_1(\zeta_1-\xi_1)E_{z5} \equiv A_1^{\mathrm{H}} \qquad (15)$$

where, for later usage, we have introduced the abbreviations A_1^{E} and A_1^{H} for the right hand sides. In order to find the unknown terms Γ_{ij}^{E}, Γ_{ij}^{H} in (14) and (15), we utilize the boundary conditions for the tangential field components in the x and y directions. Rearranging (5) and (6), with $\boldsymbol{J}=\boldsymbol{0}$, the fields are expressed as

$$\begin{bmatrix}\boldsymbol{E}\\ \boldsymbol{H}\end{bmatrix}=\frac{\mathrm{j}k_0^{-1}}{\varepsilon\mu-\xi\zeta}\begin{bmatrix}\mu & -\xi\\ -\zeta & \varepsilon\end{bmatrix}\begin{bmatrix}-\nabla_{\mathrm{T}}\times\boldsymbol{H}\\ \nabla_{\mathrm{T}}\times\boldsymbol{E}\end{bmatrix}. \qquad (16)$$

Let $\hat{\boldsymbol{\tau}}_{ij}$ be a unit-vector in the xy-plane, directed outwardly from the evaluation point and in parallel with the interface between the i:th and the j:th quadrants; see Figure 3. By using the continuity conditions $\hat{\boldsymbol{\tau}}_{ij}\cdot\boldsymbol{E}_i=\hat{\boldsymbol{\tau}}_{ij}\cdot\boldsymbol{E}_j$ and $\hat{\boldsymbol{\tau}}_{ij}\cdot\boldsymbol{H}_i=\hat{\boldsymbol{\tau}}_{ij}\cdot\boldsymbol{H}_j$ on the fields as given by (16),

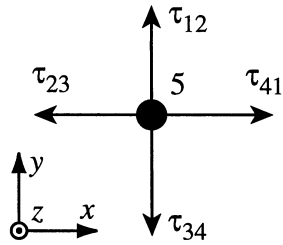

Figure 3. The tangential unit vectors used in equations (17) and (18) (cf. Figure 2 also).

it follows (after some straightforward calculations) that

$$F_j\left(\varepsilon_i\frac{\partial E_z}{\partial n_i}+\zeta_i\frac{\partial H_z}{\partial n_i}\right)+F_i\left(\varepsilon_j\frac{\partial E_z}{\partial n_j}+\zeta_j\frac{\partial H_z}{\partial n_j}\right)=0, \tag{17}$$

$$F_j\left(\mu_i\frac{\partial H_z}{\partial n_i}+\xi_i\frac{\partial E_z}{\partial n_i}\right)+F_i\left(\mu_j\frac{\partial H_z}{\partial n_j}+\xi_j\frac{\partial E_z}{\partial n_j}\right)=0, \tag{18}$$

where the abbreviations

$$F_i=\varepsilon_i\mu_i-\xi_i\zeta_i, \qquad i=1,2,3,4, \tag{19}$$

have been introduced. Now, integrating (17) along the interfaces between the quadrants and using the abbreviations introduced in (13), we obtain the following numerical approximations in all quadrants:

$$F_2\left(\varepsilon_1\Gamma^{\mathrm{E}}_{12}+\zeta_1\Gamma^{\mathrm{H}}_{12}\right)+F_1\left(\varepsilon_2\Gamma^{\mathrm{E}}_{21}+\zeta_2\Gamma^{\mathrm{H}}_{21}\right)=0, \tag{20}$$

$$F_3\left(\varepsilon_2\Gamma^{\mathrm{E}}_{23}+\zeta_2\Gamma^{\mathrm{H}}_{23}\right)+F_2\left(\varepsilon_3\Gamma^{\mathrm{E}}_{32}+\zeta_3\Gamma^{\mathrm{H}}_{32}\right)=0, \tag{21}$$

$$F_4\left(\varepsilon_3\Gamma^{\mathrm{E}}_{34}+\zeta_3\Gamma^{\mathrm{H}}_{34}\right)+F_3\left(\varepsilon_4\Gamma^{\mathrm{E}}_{43}+\zeta_4\Gamma^{\mathrm{H}}_{43}\right)=0, \tag{22}$$

$$F_1\left(\varepsilon_4\Gamma^{\mathrm{E}}_{41}+\zeta_4\Gamma^{\mathrm{H}}_{41}\right)+F_4\left(\varepsilon_1\Gamma^{\mathrm{E}}_{14}+\zeta_1\Gamma^{\mathrm{H}}_{14}\right)=0. \tag{23}$$

Repeating the procedure for (18) we obtain

$$F_2\left(\mu_1\Gamma^{\mathrm{H}}_{12}+\xi_1\Gamma^{\mathrm{E}}_{12}\right)+F_1\left(\mu_2\Gamma^{\mathrm{H}}_{21}+\xi_2\Gamma^{\mathrm{E}}_{21}\right)=0, \tag{24}$$

$$F_3\left(\mu_2\Gamma^{\mathrm{H}}_{23}+\xi_2\Gamma^{\mathrm{E}}_{23}\right)+F_2\left(\mu_3\Gamma^{\mathrm{H}}_{32}+\xi_3\Gamma^{\mathrm{E}}_{32}\right)=0, \tag{25}$$

$$F_4\left(\mu_3\Gamma^{\mathrm{H}}_{34}+\xi_3\Gamma^{\mathrm{E}}_{34}\right)+F_3\left(\mu_4\Gamma^{\mathrm{H}}_{43}+\xi_4\Gamma^{\mathrm{E}}_{43}\right)=0, \tag{26}$$

$$F_1\left(\mu_4\Gamma^{\mathrm{H}}_{41}+\xi_4\Gamma^{\mathrm{E}}_{41}\right)+F_4\left(\mu_1\Gamma^{\mathrm{H}}_{14}+\xi_1\Gamma^{\mathrm{E}}_{14}\right)=0. \tag{27}$$

Now, using all permutations of (14) and (15) to eliminate the terms in

(20)–(27) with subscripts $21, 32, 43$ and 14, we obtain

$$F_2\left(\varepsilon_1\Gamma^{\mathrm{E}}_{12}+\zeta_1\Gamma^{\mathrm{H}}_{12}\right)-F_1\left(\varepsilon_2\Gamma^{\mathrm{E}}_{23}+\zeta_2\Gamma^{\mathrm{H}}_{23}\right)=F_1\left(\varepsilon_2 A^{\mathrm{E}}_2+\zeta_2 A^{\mathrm{H}}_2\right)\equiv R^{\mathrm{E}}_1, \tag{28}$$

$$F_2\left(\mu_1\Gamma^{\mathrm{H}}_{12}+\xi_1\Gamma^{\mathrm{E}}_{12}\right)-F_1\left(\mu_2\Gamma^{\mathrm{H}}_{23}+\xi_2\Gamma^{\mathrm{E}}_{23}\right)=F_1\left(\mu_2 A^{\mathrm{H}}_2+\xi_2 A^{\mathrm{E}}_2\right)\equiv R^{\mathrm{H}}_1, \tag{29}$$

as well as their cyclic permutations; note the abbreviations R^{E}_i, R^{H}_i, $i=1,2,3,4$, introduced for the right hand sides.

Since there are two unknown field variables, E_z and H_z, at each evaluation point, our derivation must result in two separated finite difference relations. Introducing the abbreviations

$$S^{\mathrm{E}}_1=\varepsilon_1\Gamma^{\mathrm{E}}_{12}+\zeta_1\Gamma^{\mathrm{H}}_{12},\quad \text{cyclic}\ldots,\quad S^{\mathrm{H}}_1=\mu_1\Gamma^{\mathrm{H}}_{12}+\xi_1\Gamma^{\mathrm{E}}_{12},\quad \text{cyclic}\ldots,$$

we see that all permutations of (28) and (29) can be expressed as the following matrix equation:

$$\begin{bmatrix} F_2 & -F_1 & 0 & 0\\ 0 & F_3 & -F_2 & 0\\ 0 & 0 & F_4 & -F_3\\ -F_4 & 0 & 0 & F_1 \end{bmatrix}\begin{bmatrix} S^{\mathrm{E}}_1 & S^{\mathrm{H}}_1\\ S^{\mathrm{E}}_2 & S^{\mathrm{H}}_2\\ S^{\mathrm{E}}_3 & S^{\mathrm{H}}_3\\ S^{\mathrm{E}}_4 & S^{\mathrm{H}}_4 \end{bmatrix}=\begin{bmatrix} R^{\mathrm{E}}_1 & R^{\mathrm{H}}_1\\ R^{\mathrm{E}}_2 & R^{\mathrm{H}}_2\\ R^{\mathrm{E}}_3 & R^{\mathrm{H}}_3\\ R^{\mathrm{E}}_4 & R^{\mathrm{H}}_4 \end{bmatrix}. \tag{30}$$

It is readily verified that the determinant of the 4×4 matrix vanishes, i.e., (30) does not provide a unique solution. By simultaneous elimination of S^{E}_i, S^{H}_i, $i=1,2,3,4$, we then obtain the conditions on the right hand side for the existence of a (non unique) solution:

$$\frac{R^{\mathrm{E}}_1}{F_1F_2}+\frac{R^{\mathrm{E}}_2}{F_2F_3}+\frac{R^{\mathrm{E}}_3}{F_3F_4}+\frac{R^{\mathrm{E}}_4}{F_4F_1}=0, \tag{31}$$

$$\frac{R^{\mathrm{H}}_1}{F_1F_2}+\frac{R^{\mathrm{H}}_2}{F_2F_3}+\frac{R^{\mathrm{H}}_3}{F_3F_4}+\frac{R^{\mathrm{H}}_4}{F_4F_1}=0. \tag{32}$$

The conditions (31) and (32) are the finite difference equations. By back substitution through all abbreviations introduced we obtain the detailed expressions of the FDFD equations, but since they are very lengthy we do not write them out explicitly. For a biisotropic medium ($\xi\neq 0,\ \zeta\neq 0$), both of equations (31) and (32) contain E_z as well as H_z. In the isotropic case ($\xi=\zeta=0$) the equations decouple, with (31) describing the E-polarized scattering problem and with (32) describing the H-polarized scattering problem. In that case, it can be verified that the detailed expressions for the finite difference operators coincide with the expressions given in [11].

4. ABSORBING BOUNDARY CONDITION IN TERMS OF A BIE

To terminate an FDFD domain in an open region without introducing false reflections, we need an absorbing boundary condition (ABC). In this paper, we use an exact global ABC in terms of a boundary integral equation on a surface enclosing the scatterer. For our two-dimensional problem, the ABC is implemented numerically with the method of moments.

4.1. A Global ABC

In the three-dimensional case, let $\boldsymbol{F}$ denote one of the fields $\boldsymbol{E}$ or $\boldsymbol{H}$ and let the scatterer be located inside the closed surface S, having an outwardly directed unit normal $\hat{\boldsymbol{n}}$; see Figure 1. If S is sufficiently regular, it can be shown that $\boldsymbol{F}$ satisfies the following integral equation [23]

$$\frac{1}{2}\boldsymbol{F}(\boldsymbol{r}) - \oint_S \left[\left(\hat{\boldsymbol{n}}' \times \boldsymbol{F}\right) \times \nabla' G + \left(\hat{\boldsymbol{n}}' \cdot \boldsymbol{F}\right) \nabla' G + G\hat{\boldsymbol{n}}' \times (\nabla' \times \boldsymbol{F})\right] \mathrm{d}S' = \boldsymbol{F}^{\mathrm{i}}, \quad \boldsymbol{r} \text{ on } S, \tag{33}$$

where $\boldsymbol{F}^{\mathrm{i}}$ is the incident part of the field and where the integral is evaluated as a principal value integral. It thus follows that the integral equation (33) is an e act global ABC for any field $\boldsymbol{F}$ generated outside S and scattered by an object inside S.

The analogy between global ABCs in the form (33) and the global ABCs obtained in the wave-splitting approach to direct and inverse scattering problems in the time domain should be noted. For the latter, see e.g., [24] and [25] and earlier references given there. See also [26] for an example of a time domain comparison between exact and local ABCs.

4.2. MoM Approximation of the ABC and the Interlacing with the FDFD Equations

In the two-dimensional case, the z-component of the integral equation (33) becomes; see e.g., [27]

$$\frac{1}{2}F_z(\boldsymbol{r}) + \oint_\Gamma \left[G(\boldsymbol{r}, \boldsymbol{r}')\frac{\partial F_z}{\partial n'}(\boldsymbol{r}') - F_z(\boldsymbol{r}')\frac{\partial G}{\partial n'}(\boldsymbol{r}, \boldsymbol{r}')\right] \mathrm{d}\Gamma' = F_z^{\mathrm{i}}, \ \boldsymbol{r} \text{ on } \Gamma, \tag{34}$$

where Γ is the contour circumscribing the region containing the scattering cylinder and where $\frac{\partial}{\partial n'} = \hat{\boldsymbol{n}}_{\mathrm{T}} \cdot \nabla'_{\mathrm{T}}$; $\hat{\boldsymbol{n}}_{\mathrm{T}}$ is the unit normal,

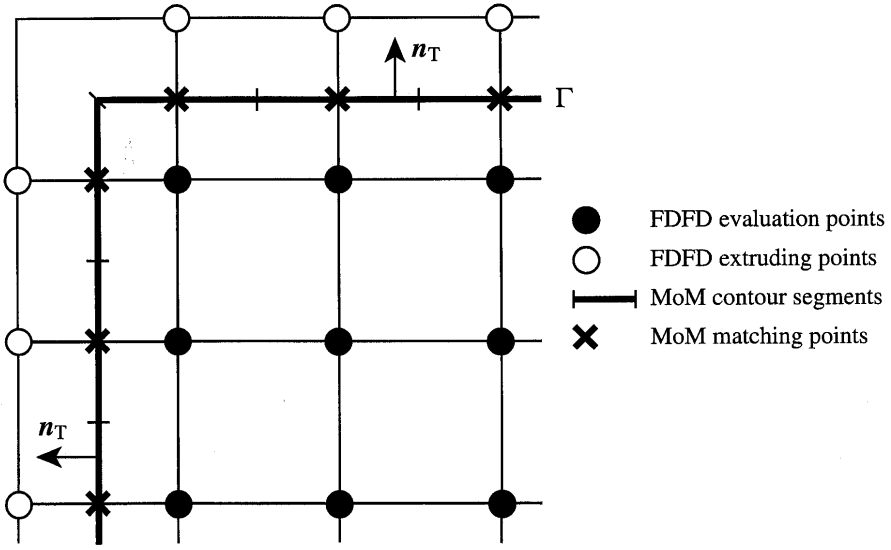

Figure 4. One corner region of the computational domain. Γ is the contour at which the global absorbing boundary condition is calculated.

in the xy plane, directed outwardly from Γ; see Figure 4. The explicit expression for the two-dimensional Green's function in (34) is

$$G(\boldsymbol{r}, \boldsymbol{r}') = -\frac{j}{4} H_0^{(2)}(k_0|\boldsymbol{r} - \boldsymbol{r}'|), \tag{35}$$

where $H_0^{(2)}$ is the zeroth order Hankel function of the second kind.

For the numerical implementation, we consider a square scattering region divided into $(N+1) \times (N+1)$ square cells. One corner of the scattering region is depicted in Figure 4, where the FDFD evaluation points, located at the intersections between the cells, are indicated with filled circles. Thus, we have in total N^2 points around which equations (31) and (32) are evaluated, which yields a total of $2N^2$ FDFD equations. However, to evaluate (31) and (32) around the FDFD points adhering to the outermost layer of cells, we need the additional values of the fields at the FDFD points indicated with blank circles in Figure 4, which results in a total of $2 \times (N^2 + 4N)$ unknowns. The additional equations, required for a unique solution, are obtained by implementing the ABC (34) for E_z and H_z, respectively.

The contour Γ, for the line-integral in (34), is located in the middle of the outermost layer of cells, as drawn by the thick solid line in Figure 4. Thus, for our theory to be valid, the constitutive

parameters in the outermost layer of cells are obliged to the vacuum values, i.e., $\varepsilon = \mu = 1$, $\xi = \zeta = 0$; see (1) and (2). For the MoM approximation, Γ is divided into $4N$ strught segments, having the length h, where on each segment the fields and their normal derivatives are constant. On the segments, the ABC (34) is enforced with point matching at the center points, indicated with crosses in Figure 4. After the numerical integration of the Green's function and its normal derivative has been carried out, see e.g., [27], we obtain at the matching points the following relation (the numerical ABC):

$$\boldsymbol{P}\bar{F}_z + \boldsymbol{Q}\partial_n\bar{F}_z = \bar{F}_z^{\mathrm{i}}, \tag{36}$$

where $\bar{F}_z$, $\partial_n\bar{F}_z$ and $\bar{F}_z^{\mathrm{i}}$ are $(4N)\times 1$ vectors containing the total field, its normal derivative and the incident field, respectively, and where $\boldsymbol{P}$ and $\boldsymbol{Q}$ are $(4N)\times(4N)$ matrices. To connect the ABC to the FDFD scheme, the elements in $\bar{F}_z$ and $\partial_n\bar{F}_z$ are approximated from the two nearest FDFD points on each side of Γ by linear interpolations and central differences, respectively, i.e.,

$$F_z \approx \frac{F_{z,\mathrm{outside}} + F_{z,\mathrm{inside}}}{2}, \tag{37}$$

$$\partial_n F_z \approx \frac{F_{z,\mathrm{outside}} - F_{z,\mathrm{inside}}}{h}. \tag{38}$$

The elements in $\bar{F}_z^{\mathrm{i}}$ are evaluated at the MoM evaluation points.

Now, we can disentangle the FDFD and MoM equations into the following linear system:

$$\begin{bmatrix} \begin{bmatrix} \boldsymbol{M}'_{\mathrm{EE}} & \boldsymbol{B} \\ \boldsymbol{C} & \boldsymbol{D} \end{bmatrix} & \begin{bmatrix} \boldsymbol{M}_{\mathrm{EH}} & \boldsymbol{0} \\ \boldsymbol{0} & \boldsymbol{0} \end{bmatrix} \\ \begin{bmatrix} \boldsymbol{M}_{\mathrm{HE}} & \boldsymbol{0} \\ \boldsymbol{0} & \boldsymbol{0} \end{bmatrix} & \begin{bmatrix} \boldsymbol{M}'_{\mathrm{HH}} & \boldsymbol{B} \\ \boldsymbol{C} & \boldsymbol{D} \end{bmatrix} \end{bmatrix} \cdot \begin{bmatrix} \begin{bmatrix} \bar{E}_{z,\mathrm{inside}} \\ \bar{E}_{z,\mathrm{outside}} \end{bmatrix} \\ \begin{bmatrix} \bar{H}_{z,\mathrm{inside}} \\ \bar{H}_{z,\mathrm{outside}} \end{bmatrix} \end{bmatrix} = \begin{bmatrix} \begin{bmatrix} \bar{0} \\ \bar{E}_z^{\mathrm{i}} \end{bmatrix} \\ \begin{bmatrix} \bar{0} \\ \bar{H}_z^{\mathrm{i}} \end{bmatrix} \end{bmatrix}, \tag{39}$$

where $\boldsymbol{M}'_{\mathrm{EE}}$, $\boldsymbol{M}_{\mathrm{EH}}$, $\boldsymbol{M}_{\mathrm{HE}}$ and $\boldsymbol{M}'_{\mathrm{HH}}$ are sparsely filled $N^2\times N^2$ matrices, describing the FDFD operators on the fields at points inside the contour Γ, and where the $N^2\times(4N)$ matrix $\boldsymbol{B}$ (that appears twice) describes the FDFD operators on the fields at points outside Γ. The matrices $\boldsymbol{C}$ and $\boldsymbol{D}$ (which also appear twice) are obtained by inserting (37) and (38) into (36) and separating the field terms evaluated at the different sides of the boundary Γ. $\boldsymbol{C}$ is a sparse $(4N)\times N^2$ matrix, as it applies only to the inner points closest to Γ, whilst $\boldsymbol{D}$ is an entirely filled $(4N)\times(4N)$ matrix. The matrices denoted $\boldsymbol{0}$ are empty matrices of suitable sizes. In the right hand side of (39), $\bar{0}$ denotes a $(N^2)\times 1$

null vector. Since, the square matrix $\boldsymbol{D}$ appears to be well-conditioned, we can rearrange in (39) whereby the fields at the interior points are obtained from the following equation:

$$\begin{bmatrix} \boldsymbol{M}_{\mathrm{EE}} & \boldsymbol{M}_{\mathrm{EH}} \\ \boldsymbol{M}_{\mathrm{HE}} & \boldsymbol{M}_{\mathrm{HH}} \end{bmatrix} \cdot \begin{bmatrix} \bar{E}_{z,\mathrm{inside}} \\ \bar{H}_{z,\mathrm{inside}} \end{bmatrix} = \begin{bmatrix} \boldsymbol{X}\bar{E}_z^{\mathrm{i}} \\ \boldsymbol{X}\bar{H}_z^{\mathrm{i}} \end{bmatrix}, \tag{40}$$

where

$$\boldsymbol{X} = -\boldsymbol{B}\boldsymbol{D}^{-1}, \tag{41}$$

$$\boldsymbol{M}_{\mathrm{EE}} = \boldsymbol{M}'_{\mathrm{EE}} + \boldsymbol{X}\boldsymbol{C}, \tag{42}$$

$$\boldsymbol{M}_{\mathrm{HH}} = \boldsymbol{M}'_{\mathrm{HH}} + \boldsymbol{X}\boldsymbol{C}. \tag{43}$$

Note that since neither $\boldsymbol{B}$ nor $\boldsymbol{C}$ nor $\boldsymbol{D}$ depend on the properties of the scatterer, the operations $\boldsymbol{X} = \boldsymbol{B}\boldsymbol{D}^{-1}$ and $\boldsymbol{X}\boldsymbol{C}$ need to be carried out only once, as long as different choices of scatterers can be confined inside the contour Γ.

5. NUMERICAL EXAMPLES

In this section, we present numerical results for the bistatic echo widths of various biisotropic cylinders. For an E-polarized incident plane wave, the co- and cross-polarized echo widths are defined as

$$\sigma_{\mathrm{co}}^{\mathrm{E}} = \lim_{r\to\infty} 2\pi r \left|\frac{E_z^{\mathrm{s}}}{E_z^{\mathrm{i}}}\right|^2, \qquad \sigma_{\mathrm{cross}}^{\mathrm{E}} = \lim_{r\to\infty} 2\pi r \left|\frac{H_z^{\mathrm{s}}}{E_z^{\mathrm{i}}}\right|^2,$$

respectively, whilst for an H-polarized incident plane wave we analogously use

$$\sigma_{\mathrm{co}}^{\mathrm{H}} = \lim_{r\to\infty} 2\pi r \left|\frac{H_z^{\mathrm{s}}}{H_z^{\mathrm{i}}}\right|^2, \qquad \sigma_{\mathrm{cross}}^{\mathrm{H}} = \lim_{r\to\infty} 2\pi r \left|\frac{E_z^{\mathrm{s}}}{H_z^{\mathrm{i}}}\right|^2,$$

respectively. For homogeneous circular cylinders, we compare the numerical results with a reference solution obtained by means of an expansion in cylindrical eigenwaves. In all numerical examples, the distances are measured in the free space wavelength, denoted λ.

5.1. Verification of the Global Absorbing Boundary Condition

To check the numerical accuracy of the global ABC, we consider the electric field radiated by an electric line source in an empty space ($\varepsilon = \mu = 1,\ \xi = \zeta = 0$). The computational region contains 41×41

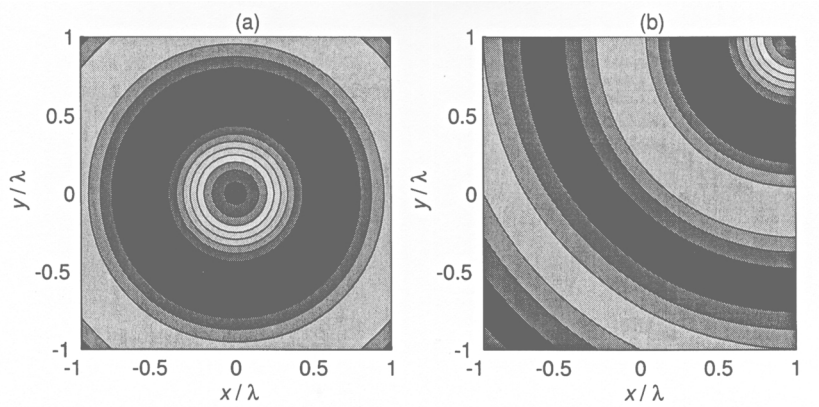

Figure 5. The electric field radiated by an electric line source in (a) $x = y = 0$; (b) $x = y = \lambda$.

interior FDFD points (i.e., $N = 41$) with the spacing $h = 0.05\lambda$ in both the x and y directions. If the ABC works properly, a contour plot of the instantaneous electric field in the computational region shall exhibit circular rings centered around the position of the line source. The results when the line source is located in $x = y = 0$ (the central FDFD point) and in $x = y = \lambda$ (one of the corner FDFD points) are depicted in Figures 5(a) and 5(b), respectively, and we see that the level curves are very close to circular. Thus, we conclude that the ABC is reliable both when the source is located well inside the region and, especially, when the source is located very close to the boundary.

5.2. Circular Dielectric Cylinder

We consider an isotropic dielectric cylinder with the radius $a = \lambda$ and the parameters $\varepsilon = 2.0$, $\mu = 1.0$, $\kappa = \chi = 0$ (hence there will be no cross polarized scattering, i.e., $\sigma^{\mathrm{E}}_{\mathrm{cross}} = \sigma^{\mathrm{H}}_{\mathrm{cross}} = 0$). For the computational region we consider two different mesh sizes, 41×41 FDFD points with spacing $h = 0.05\lambda$ and 81×81 FDFD points with spacing $h = 0.025\lambda$ (in both cases the square region is truncated as close as possible to the cylinder). For comparison, we use the same values of ε, a and h as in [11]. The echo widths $\sigma^{\mathrm{E}}_{\mathrm{co}}$ and $\sigma^{\mathrm{H}}_{\mathrm{co}}$ for waves impinging in the direction $\phi = 0$ (the $+x$ direction) are depicted in Figures 6(a) and 6(b), respectively, where the solid lines depict the reference solution, the dotted lines depict the FDFD-BIE results using $h = 0.05\lambda$ and the dashed lines depict the FDFD-BIE results using $h = 0.025\lambda$.

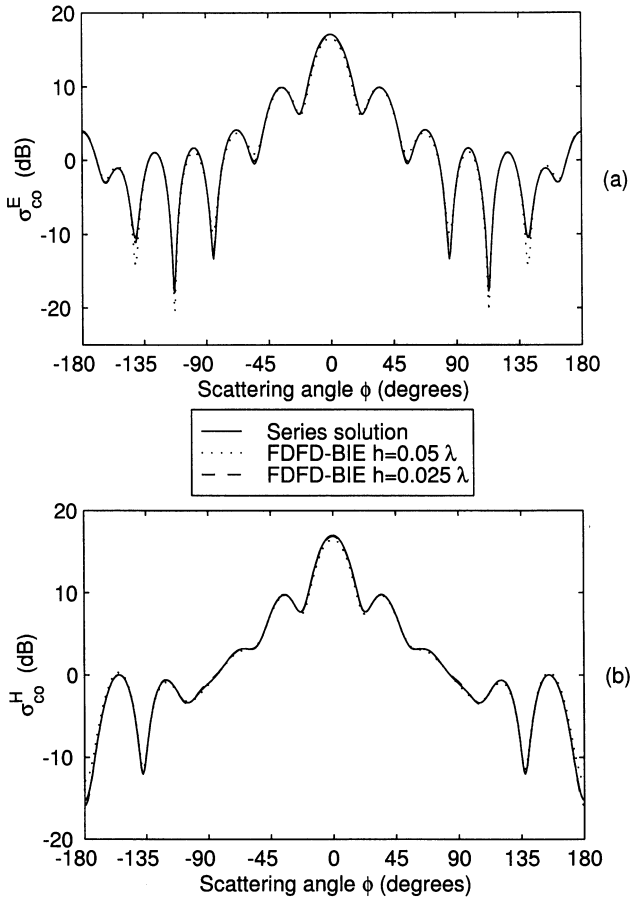

Figure 6. The bistatic echo widths for a dielectric circular cylinder with the radius $a = \lambda$ and the parameters $\varepsilon = 2,\ \mu = 1$. The cylinder is illuminated in the direction $\phi = 0°$.

We observe very good agreements with the reference solutions when $h = 0.025\lambda$ whilst smaller deviations occur when $h = 0.05\lambda$. In both cases, our results are in better agree- ment with the reference solution than the ones presented in [11], which were calculated with the same type of FDFD scheme but with a local ABC (cf. the time domain com- parison in [26] between global and local ABCs). We also made comparisons (with good agreement) with results reported in [11] for cylinders with non-circular cross-sections but, due to space reasons, our results are not presented here.

5.3. Circular Chiral Cylinder and Circular Tellegen Cylinder

It is pertinent to express the magnetoelectric cross-coupling parameters as $\xi = \chi - \mathrm{j}\kappa$ and $\zeta = \chi + \mathrm{j}\kappa$, where κ is the chirality parameter and χ is the non-reciprocity (Tellegen) parameter; see e.g., [19]. First, we consider a purely chiral circular cylinder with the radius $a = \lambda$ and the parameters $\varepsilon = 2.6 - 0.2\mathrm{j}$, $\mu = 1.5 - 0.1\mathrm{j}$, $\kappa = 0.6 - 0.1\mathrm{j}$ and $\chi = 0$. Note that the parameters are complex valued, since it is reasonable to assume that the chiral medium is lossy in the frequency region of interest; see Chapter 6 in [19]. The numerical parameters are the same as in the previous case, i.e., $N = 41$, $h = 0.05\lambda$ and $N = 81$, $h = 0.025\lambda$, respectively. The echo widths $\sigma^{\mathrm{E}}_{\mathrm{co}}$ and $\sigma^{\mathrm{H}}_{\mathrm{co}}$ for waves impinging in the direction $\phi = 0$ are depicted in Figures 7(a) and 7(b), respectively, with the solid lines for the reference solution, the dotted lines for $h = 0.05\lambda$ and the dashed lines for $h = 0.025\lambda$. From reciprocity and the circular symmetry it follows that $\sigma^{\mathrm{E}}_{\mathrm{cross}} = \sigma^{\mathrm{H}}_{\mathrm{cross}}$ which was also verified numerically; the results are depicted in Figure 7(c). All numerical results in Figure 7 are in good agreements with the reference solutions, although the errors seem somewhat larger than the ones observed in the isotropic case, which is probably related to the fact that the chiral medium has a larger refraction index, resulting in shorter wavelengths than in the isotropic medium.

Next, we switch to a non-reciprocal Tellegen cylinder by setting $\kappa = 0$ and $\chi = 0.6 - 0.1\mathrm{j}$; all other parameters are unchanged. $\sigma^{\mathrm{E}}_{\mathrm{co}}$ and $\sigma^{\mathrm{H}}_{\mathrm{co}}$ are depicted in Figures 8(a) and 8(b), respectively, with the solid lines for the reference solution, the dotted lines for $h = 0.05\lambda$ and the dashed lines for $h = 0.025\lambda$. Lacking a rigorous argument, based on e.g., reciprocity, the numerical results, depicted in Figure 8(c), indicate however that $\sigma^{\mathrm{E}}_{\mathrm{cross}} = \sigma^{\mathrm{H}}_{\mathrm{cross}}$. Also for the Tellegen cylinder the numerical results are in good agreement with the reference solutions.

Comparing Figures 7(c) and 8(c), we notice that (with the same values of the featuring parameters) the Tellegen cylinder yields considerably smaller cross-polarized scattering than the chiral cylinder. The reason is that eigenwaves in homogeneous Tellegen media have the same phase velocity (cf. Equation (A3) in the Appendix A) and hence there will be no rotation of the polarization plane as the total wave propagates. On the other hand, the eigenwaves in chiral media propagates with different velocities, which results in a continuous shift of the polarization plane as the wave propagates; see page 36 in [19]. Thus, the Tellegen parameter contributes to the cross-polarization only by means of scattering from inhomogeneous regions (in this example, the boundary of the cylinder). This conclusion is readily verified from

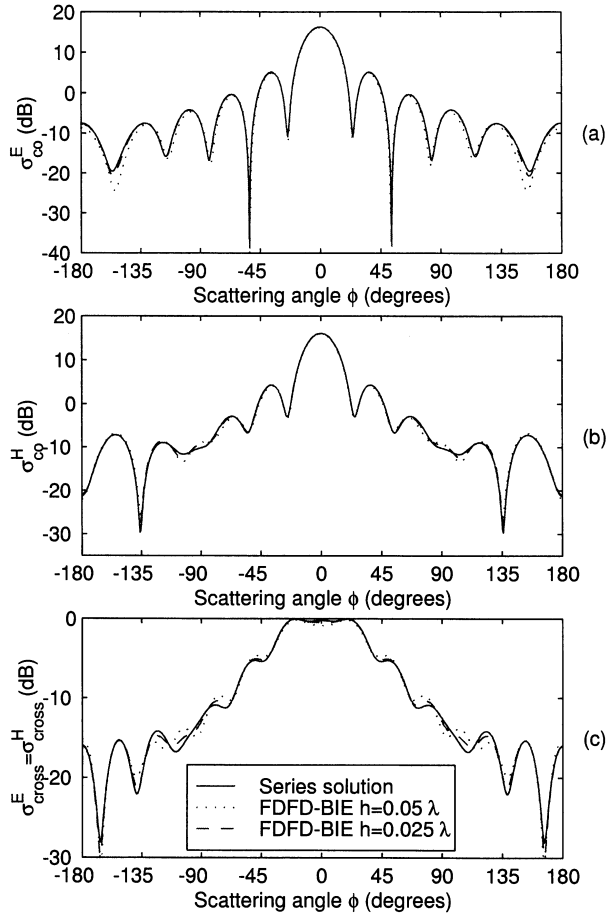

Figure 7. The bistatic echo widths for a chiral circular cylinder with the radius $a = \lambda$ and the parameters $\varepsilon = 2.6 - 0.2\mathrm{j}$, $\mu = 1.5 - 0.1\mathrm{j}$ and $\kappa = 0.6 - 0.1\mathrm{j}$. The cylinder is illuminated in the direction $\phi = 0°$.

equations (31) and (32) which are seen to decouple in a homogeneous Tellegen medium, as indicated by equations (14) and (15), in which there is no crosscoupling between E_z and H_z when $\xi = \zeta = \chi$.

5.4. Cylinder Having Non-circular Cross-section

Now, we consider a piecewise homogeneous cylinder consisting of three subcylinders with identical material properties; two quadratic cylinders both having the dimensions $0.3\lambda \times 0.3\lambda$ and one rectangular cylinder

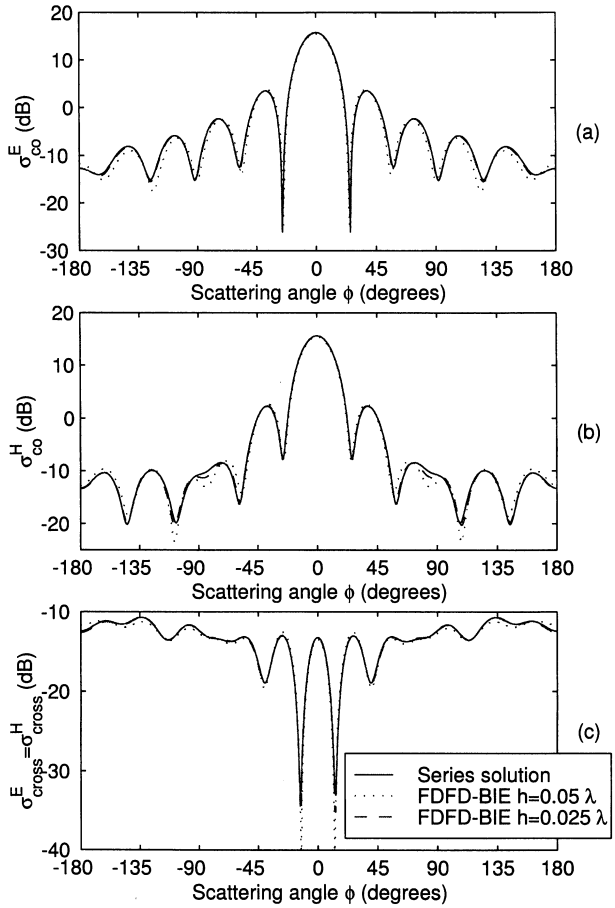

Figure 8. The bistatic echo widths for a circular Tellegen cylinder with the radius $a = \lambda$ and the parameters $\varepsilon = 2.6 - 0.2\text{j}$, $\mu = 1.5 - 0.1\text{j}$ and $\chi = 0.6 - 0.1\text{j}$. The cylinder is illuminated in the direction $\phi = 0°$.

with the dimensions $0.2\lambda \times \lambda$. The locations of the subcylinders are depicted in Figure 9. The size of the computational region is $\lambda \times \lambda$ (measured over the interior FDFD points) and we consider two different mesh sizes, 21×21 FDFD points with spacing $h = 0.05\lambda$ (as drawn in Figure 9) and 41×41 FDFD points with spacing $h = 0.025\lambda$. The incident plane wave propagates in the direction $\phi = 45°$. The echo-ndths for a chiral multi-cylinder, with the constitutive parameters $\varepsilon = 2.6 - 0.2\text{j}$, , $\mu = 1.5 - 0.1\text{j}$, $\kappa = 0.6 - 0.1\text{j}$, $\chi = 0$, are depicted in figure 10 and the echo-widths for a Tellegen multi-cylinder, with the constitutive

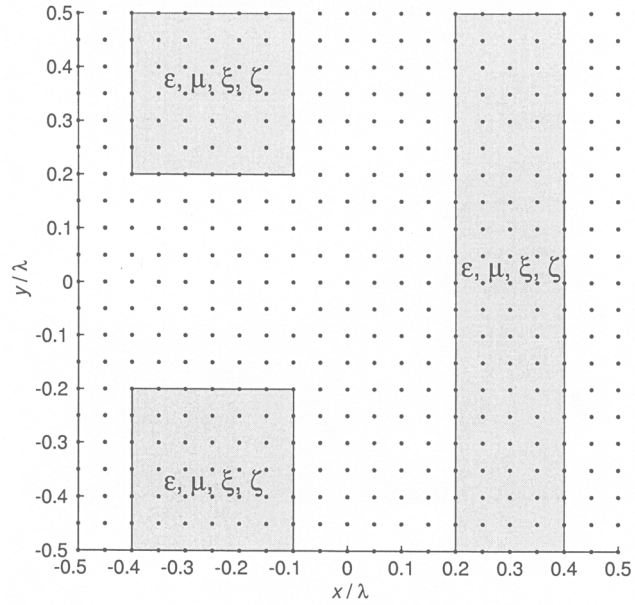

Figure 9. The location of a biisotropic multi-cylinder configuration in a FDFD mesh with 21×21 interior points.

parameters $\varepsilon = 2.6 - 0.2\mathrm{j}$, $\mu = 1.5 - 0.1\mathrm{j}$, $\chi = 0.6 - 0.1\mathrm{j}$, $\kappa = 0$, are depicted in Figure 11, where (in both figures) the the dashed lines depict the FDFD-BIE results using $h = 0.05\lambda$ and the solid lines depict the FDFD-BIE results using $h = 0.025\lambda$.

From Figures 10(c) and 10(d), we see that $\sigma^{\mathrm{E}}_{\mathrm{cross}} \neq \sigma^{\mathrm{H}}_{\mathrm{cross}}$ for the chiral cylinder, which can be understood from the lack of circular symmetry. However, it is more interesting to note that for the Tellegen cylinder the numerical results, depicted in Figure 11(c), indicate that we still have $\sigma^{\mathrm{E}}_{\mathrm{cross}} = \sigma^{\mathrm{H}}_{\mathrm{cross}}$ even though the cylinder is not circular in the cross-section.

We also made comparisons (with good agreement) with results reported in [3] for chiral cylinders and with results reported in [20] for truly biisotropic cylinders but, due to space reasons, the results cannot be presented here.

As a final example, we investigate numerically some consequences of the non-reciprocity parameter χ. From Lorentz reciprocity theorem (see e.g., [28]) it follows, in the two-dimensional case, that if the scatterer inside the ABC contour γ consists of a reciprocal material

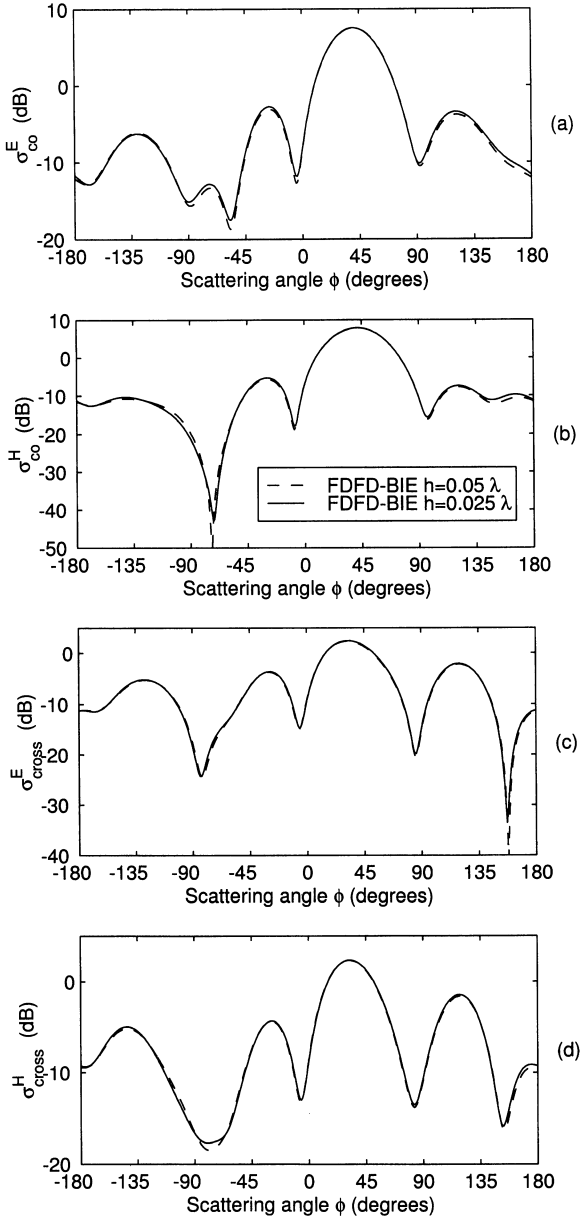

Figure 10. The bistatic echo widths for a chiral multi-cylinder with the geometry given in Figure 9; the parameters are $\varepsilon = 2.6 - 0.2\text{j}$, $\mu = 1.5 - 0.1\text{j}$ and $\kappa = 0.6 - 0.1\text{j}$. The cylinder is illuminated in the direction $\phi = 45°$.

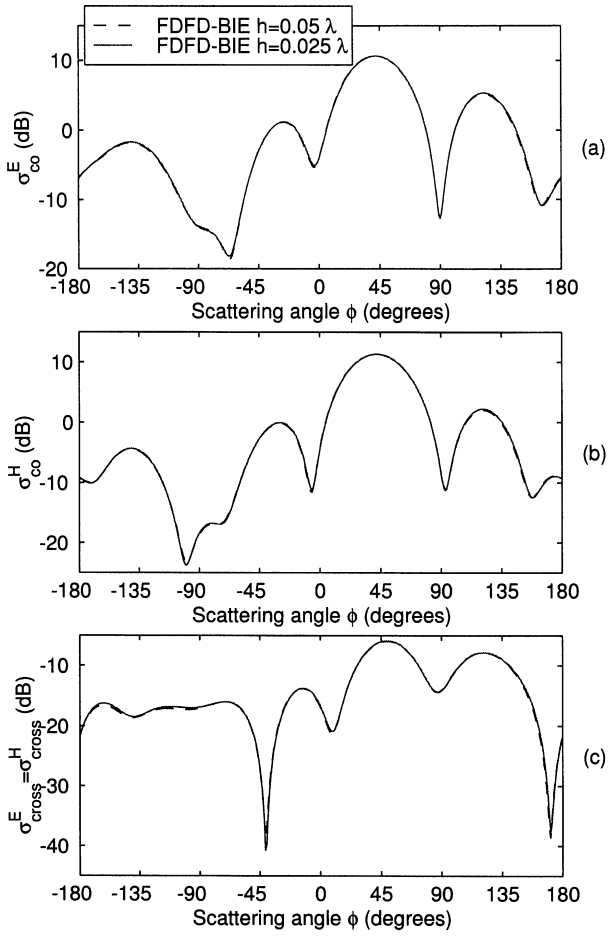

Figure 11. The bistatic echo widths for a Tellegen multi-cylinder with the geometry given in Figure 9; the parameters are $\varepsilon = 2.6 - 0.2\mathrm{j}$, $\mu = 1.5 - 0.1\mathrm{j}$ and $\chi = 0.6 - 0.1\mathrm{j}$. The cylinder is illuminated in the direction $\phi = 45°$.

and if there are no sources inside Γ, the following quantity:

$$R = \oint_{\Gamma} \left(E_z^{(1)} \frac{\partial E_z^{(2)}}{\partial n} - E_z^{(2)} \frac{\partial E_z^{(1)}}{\partial n} - H_z^{(1)} \frac{\partial H_z^{(2)}}{\partial n} + H_z^{(2)} \frac{\partial E_z^{(1)}}{\partial n} \right) \mathrm{d}\Gamma \tag{44}$$

is identically zero. In (44), $\{E_z^{(1)}, H_z^{(1)}\}$ and $\{E_z^{(2)}, H_z^{(2)}\}$ are the z-

Table 1. The measure R of non-reciprocity, evaluated with different values of the mesh parameter h, for the case with two electric line sources.

	$\kappa = 0.6 - 0.1\text{j},\ \chi = 0$	$\kappa = 0,\ \chi = 0.6 - 0.1\text{j}$
$h = 0.05\lambda$	$0.0507 + 0.0416\text{j}$	$0.0849 + 0.1162\text{j}$
$h = 0.025\lambda$	$0.0134 + 0.0112\text{j}$	$0.0186 + 0.0324\text{j}$
$h = 0.0125\lambda$	$0.0034 + 0.0029\text{j}$	$0.0043 + 0.0084\text{j}$

Table 2. The measure R of non-reciprocity, evaluated with different values of the mesh parameter h, for the case with one electric line source and one magnetic line source.

	$\kappa = 0.6 - 0.1\text{j},\ \chi = 0$	$\kappa = 0,\ \chi = 0.6 - 0.1\text{j}$
$h = 0.05\lambda$	$-0.0380 - 0.0747\text{j}$	$3.5828 - 6.5857\text{j}$
$h = 0.025\lambda$	$-0.0081 - 0.0211\text{j}$	$3.8219 - 6.6851\text{j}$
$h = 0.0125\lambda$	$-0.0018 - 0.0055\text{j}$	$3.8826 - 6.7119\text{j}$

components of the fields generated by two different sources located outside of Γ. The numerical values of R, obtained using three different values of the mesh parameter h, are given in Tables 1 and 2, for both the chiral cylinder and the Tellegen cylinder of this subsection. The results of Table 1 were obtained when source nr.1 was an electric line source in the point $(2\lambda, 0)$ and source nr.2 an electric line source in the point $(0, 2\lambda)$, with both sources having a unit strength.

We see in Table 1 that for both the chiral cylinder and the Tellegen cylinder R tends to zero as h decreases, i.e., the integral in (44) is in agreement with the fact that the chiral medium is reciprocal but the integral gives little indication that the Tellegen medium is non-reciprocal. The results of table 2 were obtained when source nr.1 was an electric line source in the point $(-2\lambda, 0)$ and source nr.2 a magnetic line source in the point $(0, -2\lambda)$. with both sources having a unit strength.

In Table 2, we see that for the chiral cylinder R tends to zero as h decreases whilst for the Tellegen cylinder R instead seems to converge towards a non-zero value, i.e., the integral in (44) indicates that the Tellegen material is non-reciprocal.

6. DISCUSSION AND CONCLUSIONS

The scattering problem for inhomogeneous two-dimensional biisotropic cylinders has been considered. Finite difference equations for the interior region as well as a contour integral equation realizing a global absorbing boundary condition have been derived and implemented numerically. Comparisons with an exact series solution have been made for the circular cylinder case and for other cases comparisons have been made with results found in the literature. The influences of the chirality and non-reciprocity parameters on the scattering properties have been investigated and the results are in accordance with what can be expected from theoretical results in the literature [19].

Even though the ABC contributes with a filled submatrix, the total matrix in equation (43) is sparse. Computationally, the present FDFD-BIE method is thus much faster than a moment method [3] using a filled matrix of the same size. Hence, the present method can be used for solving 2D scattering problems involving scatterers of intermediate sizes (i.e., a couple of wavelengths) in both directions whereas MoM under, the same computation time, only can be used for considerably smaller or thinner structures.

With a local ABC, the matrix in (43) would be even sparser. Thus, the present method is computationally slower than methods using a local ABC like PML [7] or MEI [10], but the results from Subsection 5.1 indicate that our global ABC is reliable for all possible scatterers inside the domain and the results from Subsection 5.2 indicate that our ABC should yield more accurate results than what can be obtained with MEI. With a known shape of the scatterer, like in e.g., a direct problem, the dense submatrix from the global ABC can be minimized if the contour Γ in (34) is chosen as the rectangle with the smallest possible circumference that can enclose the scatterer.

With a surface integral formulation for the global ABC, the ABC might suffer from the problem with interior resonances at a sequence of discrete frequencies. To investigate this aspect, we tried with several different sizes of a computational domain containing vacuum, but the problem with resonances never any of these numerical test.

Since our ABC is unlikely to generate artifacts from the boundary in the solution, the usefulness of the hybrid method as a fast solver in an optimization approach for solving the corresponding inverse problem is of interest for forthcoming research. The usefulness of an extension of the hybrid method to the three-dimensional case is of interest also.

APPENDIX A. ABOUT THE EXACT SOLUTION FOR A HOMOGENEOUS CIRCULAR CYLINDER

In this appendix, we give a short outline on the exact series solution, which was used as a benchmark for the numerical solution. The series solution, in terms of cylindrical eigenwaves, for a single chiral circular cylinder can be found in [29] and we merely sketch the extension of that solution to include the non-reciprocity parameter also. It should be mentioned also that an extension of the solution in [29] to a multilayered chiral cylinder can be found in [30] and that a three-dimensional series solution for the biisotropic sphere is available in [21].

In a biisotropic medium, Maxwell's equations can be written in the compact form

$$\nabla \times \begin{bmatrix} \boldsymbol{E} \\ \boldsymbol{H} \end{bmatrix} = \mathrm{j}\omega \begin{bmatrix} -(\chi + \mathrm{j}\kappa) & -\mu \\ \varepsilon & (\chi - \mathrm{j}\kappa) \end{bmatrix} \begin{bmatrix} \boldsymbol{E} \\ \boldsymbol{H} \end{bmatrix}. \tag{A1}$$

By diagonalizing the matrix in (A1), we obtain the eigenwaves, denoted $\boldsymbol{Q}^+$ and $\boldsymbol{Q}^-$, in a homogeneous biisotropic medium. The eigenwaves satisfy the equations

$$\nabla \times \boldsymbol{Q}^+ = k^+ \boldsymbol{Q}^+, \qquad \nabla \times \boldsymbol{Q}^- = -k^- \boldsymbol{Q}^-, \tag{A2}$$

in which the wavenumbers $k^\pm$ are

$$k^+ = \omega \left(\sqrt{\varepsilon\mu - \chi^2} + \kappa \right), \qquad k^- = \omega \left(\sqrt{\varepsilon\mu - \chi^2} - \kappa \right). \tag{A3}$$

The fields $\boldsymbol{E}$ and $\boldsymbol{H}$ can be expressed in terms of the eigenwaves as

$$\begin{bmatrix} \boldsymbol{E} \\ \boldsymbol{H} \end{bmatrix} = \begin{bmatrix} 1 & 1 \\ \mu^{-1} \left(\mathrm{j}\sqrt{\varepsilon\mu - \chi^2} - \chi \right) & -\mu^{-1} \left(\mathrm{j}\sqrt{\varepsilon\mu - \chi^2} + \chi \right) \end{bmatrix} \begin{bmatrix} \boldsymbol{Q}^+ \\ \boldsymbol{Q}^- \end{bmatrix}. \tag{A4}$$

From (A2), it follows that the eigenwaves satisfy the Helmholtz equations

$$\nabla^2 \boldsymbol{Q}^\pm + \left(k^\pm \right)^2 \boldsymbol{Q}^\pm = 0, \tag{A5}$$

and by solving for the z-components in a plane-polar coordinate system (ρ, ϕ) (i.e., in the two-dimensional case) we obtain the following series solutions in terms of cylindrical eigenwaves:

$$Q_z^\pm = \sum_{n=-\infty}^{\infty} A_n^\pm \mathrm{J}_n \left(k^\pm \rho \right) \exp(\mathrm{j}n\phi), \tag{A6}$$

in which J_n denotes the the n:th order Bessel function of the first kind. Finally, the expansion coefficients $\{A_n^{\pm}\}_{n=-\infty}^{\infty}$ are determined via equation (A4) by enforcing the continuity conditions at the interface $\rho = a$ on the in- and out-going eigenwaves in the region exterior to the cylinder.

REFERENCES

1. Harrington, R. F., *Field Computation by Moment Methods,* Macmillan, New York, 1968.
2. Wang, J. J. H., *Generalized Moment Methods in Electromagnetics,* Wiley, New York, 1991.
3. Kluskens, M. S. and E. H. Newman, "Scattering by a chiral cylinder of arbitrary cross section," *IEEE Trans. Ant. Prop.,* Vol. 38, No. 9, 1448–1455, September 1990.
4. Cheng, D. and W. Lin, "New theorems for bianisotropic media," *Int. J. Infrared and MM Waves,* Vol. 13, No. 3, 351–359, March 1992.
5. Berenger, J. P., "A perfectly matched layer for the absorption of electromagnetic waves," *J. Comp. Phys.,* Vol. 114, No. 2, 185–200, October 1994.
6. Pekel, U. and R. Mittra, "A finite-element frequency-domain application of the perfectly matched layer (PML) concept," *Microwave and Opt. Tech. Letters,* Vol. 9, No. 3, 117–121, June 1995.
7. Rappaport, C. M., "Interpreting and improving the PML absorbing boundary condition using anisotropic lossy mapping of space," *IEEE Trans. Magn.,* Vol. 32, No. 3, 968–974, May 1996.
8. González García, S., I. Villó Pérez, R. Gómez Martín, and B. García Olmedo, "Extension of Berenger's PML for bi-isotropic media," *IEEE Microw. Guided Wave Lett.,* Vol. 8, No. 9, 297–299, September 1998.
9. Kuzuoglu, M. and R. Mittra, "A systematic approach to the derivation of constitutive parameters of a perfectly matched absorber," *IEEE Microw. Guided Wave Lett.,* Vol. 8, No. 9, 313–315, June 1998.
10. Mei, K. K., R. Pous, Z. Chen, Y.-W. Liu, and M. D. Prouty, "Measured equation of invariance: a new concept in field computations," *IEEE Trans. Ant. Prop.,* Vol. 42, No. 3, 320–328, March 1994.
11. Hong, W., Y. W. Liu, and K. K. Mei, "Application of the

measured equation of invariance to solve scattering problems involving a penetrable medium," *Radio Science,* Vol. 29, No. 4, 897–906, July–August 1994.

12. Chen, J. and W. Hong, "EM scattering analysis of a ferrite cylinder by a FD-FD technique with an effective absorbing boundary condition and MEI," *Int. J. Infrared and Millimeter Waves,* Vol. 16, No. 12, 2209–2221, 1995.
13. Cermak, I. A. and P. Silvester, "Solution of 2-dimensional field problems by boundary relaxation," *Proc. IEE,* Vol. 115, No. 9, 1341–1348, September 1968.
14. McDonald, B. H. and A. Wexler, "Finite-element solution of unbounded field problems," *IEEE Trans. Microw. Theory Tech.,* Vol. 20, No. 12, 841–847, December 1972.
15. Jin, J. M., J. L. Volakis, and J. D. Collins, "A finite-element-boundary-integral method for scattering and radiation by two- and three-dimensional structures," *IEEE Ant. Prop. Mag.,* Vol. 33, No. 3, 22–32, June 1991.
16. Sheng, X.-Q., J. M. Jin, J. Song, C. C. Lu, and W. C. Chew, "On the formulation of hybrid finite-element and boundary-integral methods for 3-D scattering," *IEEE Trans. Ant. Prop.,* Vol. 46, No. 3, 303–311, March 1998.
17. Rogier, H., F. Olyslager, and D. De Zutter, "A new hybrid FDTD-BIE approach to model electromagnetic scattering problems," *IEEE Microw. Guided Wave Lett.,* Vol. 8, No. 3, 138–140, March 1998.
18. Song, J., C.-C. Lu, and W. C. Chew, "Multilevel fast multipole algorithm for electromagnetic scattering by large complex objects," *IEEE Trans. Ant. Prop.,* Vol. 45, No. 10, 1488–1493, October 1997.
19. Lindell, I. V., A. H. Sihvola, S. A. Tretyakov, and A. J. Viitanen, *Electromagnetic Waves in Chiral and Bi-Isotropic Media,* Artech House, Boston & London, 1994.
20. Monzon, J. C., "Scattering by a biisotropic body," *IEEE Trans. Ant. Prop.,* Vol. 43, No. 11, 1288–1296, November 995.
21. He, S. and J. Cao, "Scattering from a biisotropic object of arbitrary shape," *J. Electromagnetic Waves and Applic.,* Vol. 12, No. 12, 1547–1574, December 1998.
22. Lindell, I. V., A. H. Sihvola, P. Puska, and L. H. Ruotanen, "Conditions for the parameter dyadics of lossless bianisotropic media," *Microwave and Opt. Tech. Letters,* Vol. 8, No. 5, 268–272, April 1995.

23. Strom, S., "Introduction to integral representations and integral equations for time-harmonic acoustic, electromagnetic and elastodynamic wave fields," *Field Representations and Introduction to Scattering,* V. V. Varadan, A. Lakhtakia, and V. K. Varadan (eds.), Vol. 1, Elsevier Science Publ., 1991.
24. Weston, V. H., "Factorization of the wave equation in a nonplanar stratified medium," *J. Math. Phys.,* Vol. 29, No. 1, 36–45, January 1988.
25. Weston, V. H., "Time-domain wave splitting of Maxwell's equations," *J. Math. Phys.,* Vol. 34, No. 4, 1370–1392, April 1993.
26. Cao, J. and S. He, "An exact absorbing boundary condition and its application to three-dimensional scattering from thin dispersive structures," *J. Acoust. Soc. Am.,* Vol. 99, No. 4, 1854–1861, April 1996.
27. Morita, N., N. Kumagai, and J. R. Mautz, *Integral Equation Methods for Electromagnetics,* Artech House, Boston & London, 1990.
28. Collin, R. E., *Foundations for Microwave Engineering,* 62–64, New York, McGraw-Hill, 1992.
29. Bohren, C. F., "Scattering of electromagnetic waves by an optically active cylinder," *J. Colloid Interface Sci.,* Vol. 66, 105–109, August 1978.
30. Kluskens, M. S. and E. H. Newman, "Scattering by a multilayer chiral cylinder," *IEEE Trans. Ant. Prop.,* Vol. 39, No. 1, 91–96, March 1991.